

Article

Signal-to-Noise Ratio Analysis for the Voltage-Mode Read-Out of Quartz Tuning Forks in QEPAS Applications

Michele Di Gioia^{1,2}, Luigi Lombardi² , Cristoforo Marzocca^{2,*}, Gianvito Matarrese², Giansergio Menduni¹, Pietro Patimisco¹  and Vincenzo Spagnolo^{1,2} 

¹ PolySense Lab, Dipartimento Interateneo di Fisica, University and Politecnico of Bari, Via Amendola 173, 70126 Bari, Italy

² Dipartimento di Ingegneria Elettrica e Dell'Informazione, Politecnico of Bari, Via Edoardo Orabona 4, 70126 Bari, Italy

* Correspondence: cristoforo.marzocca@poliba.it; Tel.: +39-080-5963313

Abstract: Quartz tuning forks (QTFs) are employed as sensitive elements for gas sensing applications implementing quartz-enhanced photoacoustic spectroscopy. Therefore, proper design of the QTF read-out electronics is required to optimize the signal-to-noise ratio (SNR), and in turn, the minimum detection limit of the gas concentration. In this work, we present a theoretical study of the SNR trend in a voltage-mode read-out of QTFs, mainly focusing on the effects of (i) the noise contributions of both the QTF-equivalent resistor and the input bias resistor R_L of the preamplifier, (ii) the operating frequency, and (iii) the bandwidth (BW) of the lock-in amplifier low-pass filter. A MATLAB model for the main noise contributions was retrieved and then validated by means of SPICE simulations. When the bandwidth of the lock-in filter is sufficiently narrow ($BW = 0.5$ Hz), the SNR values do not strongly depend on both the operating frequency and R_L values. On the other hand, when a wider low-pass filter bandwidth is employed ($BW = 5$ Hz), a sharp SNR peak close to the QTF parallel-resonant frequency is found for large values of R_L ($R_L > 2$ M Ω), whereas for small values of R_L ($R_L < 2$ M Ω), the SNR exhibits a peak around the QTF series-resonant frequency.



Citation: Di Gioia, M.; Lombardi, L.; Marzocca, C.; Matarrese, G.; Menduni, G.; Patimisco, P.; Spagnolo, V. Signal-to-Noise Ratio Analysis for the Voltage-Mode Read-Out of Quartz Tuning Forks in QEPAS Applications. *Micromachines* **2023**, *14*, 619. <https://doi.org/10.3390/mi14030619>

Academic Editors: Luigi Sirleto and Giancarlo C. Righini

Received: 7 February 2023

Revised: 3 March 2023

Accepted: 4 March 2023

Published: 8 March 2023



Copyright: © 2023 by the authors. Licensee MDPI, Basel, Switzerland. This article is an open access article distributed under the terms and conditions of the Creative Commons Attribution (CC BY) license (<https://creativecommons.org/licenses/by/4.0/>).

Keywords: quartz-enhanced photoacoustic spectroscopy; quartz tuning fork; voltage-mode read-out; front-end electronics; signal-to-noise ratio; gas sensing

1. Introduction

Quartz-enhanced photoacoustic spectroscopy (QEPAS) is a well-known technique used for the detection of specific trace gases in complex mixtures [1–7]. The high performances in terms of selectivity and sensitivity allow for the exploitation of this technique in a wide range of applications, such as environmental monitoring [8–10], chemical analysis [11,12], and advanced biomedical diagnostics [13,14]. In QEPAS, acoustic waves are generated between the prongs of a quartz tuning fork (QTF) by the absorption of modulated light from the gas molecules, via non-radiative relaxation processes [2,15]. QTFs are employed as piezoelectric sensitive elements to transduce pressure waves in an electric signal [2,6]. This technique was firstly introduced in 2002 and exploited standard QTFs resonating at 32 kHz [16]. These quartz resonators are characterized by a good immunity to environmental acoustic noise because of their high quality factors (Q) and compact dimensions. Due to the sharp resonance, external noise sources outside of the resonator's small bandwidth (~4 Hz at atmospheric pressure) do not influence the QTF signal [17].

Suitable front-end electronics must be designed to read-out the signal generated by the QTF. The common read-out architecture employed in QEPAS sensors is the transimpedance amplifier (TIA) [8–14], schematically depicted in Figure 1.

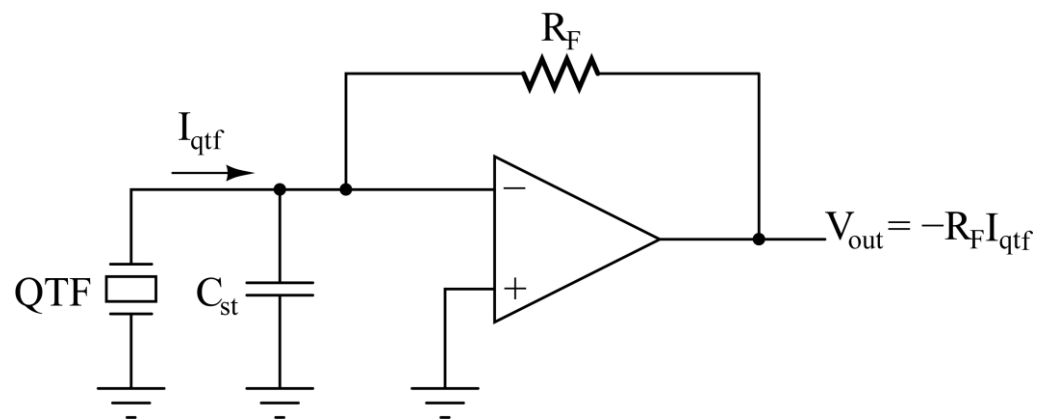


Figure 1. QTF read-out by means of a transimpedance preamplifier.

In this configuration, the current generated by the QTF (I_{qtf}) due to the charge displacement caused by piezoelectric effect when pressure waves put prongs in vibration is forced to flow entirely in the feedback resistor R_F . Due to the virtual ground established on the inverting node of the operational amplifier (OPAMP), the measurement is insensitive to the stray capacitance C_{st} and, in turn, the output voltage (V_{out}) is proportional to I_{qtf} .

Recently, it has been demonstrated that a voltage-mode approach for the read-out electronics of QTFs can be advantageous in terms of signal-to-noise ratio (SNR) [18–21]. In this case, the piezoelectric transducer is coupled to a voltage amplifier, realized by means of a classic OPAMP in a non-inverting configuration, as illustrated in Figure 2, and characterized by very high input impedance. Since the QTF is an open circuit at DC, a load resistor R_L must necessarily be connected to the non-inverting input of the amplifier to establish its DC voltage to ground, when the input bias current of the OPAMP can be neglected.

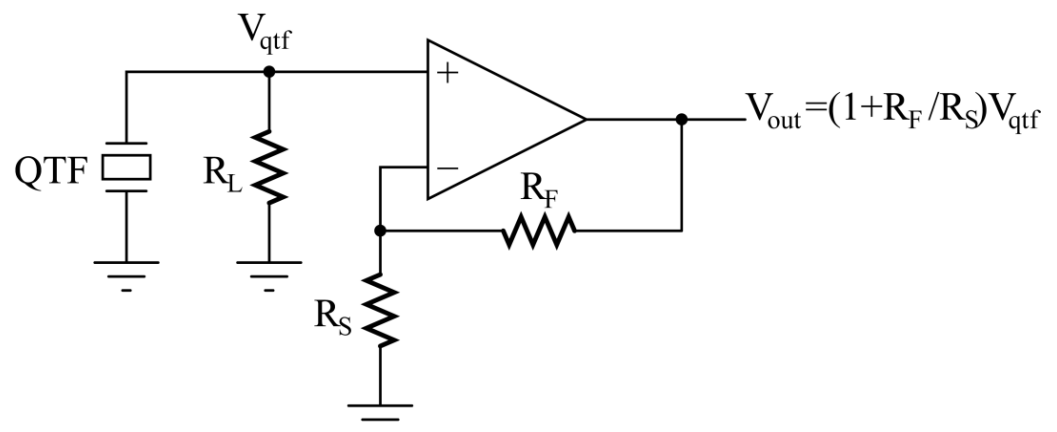


Figure 2. Voltage-mode read-out of the QTF (OPAMP in non-inverting configuration).

The thermal noise of the resistor R_L contributes to the overall noise spectral density of the circuit output. Furthermore, the QTF experiences the loading effect due to R_L ; then, the input voltage V_{qtf} of the amplifier results from the product of the current generated by the QTF under this load and the value of R_L itself. As a consequence, R_L has a direct impact on both the level of the useful signal V_{out} and the noise at the output of the preamplifier.

QEPAS requires synchronous detection techniques based on lock-in amplifiers (LIAs) to efficiently extract the useful signal component from the noise floor [2,22–26]. In LIAs, the amplifier signal is first multiplied with both a sinewave and a 90° phase-shifted copy of that sinewave at a selected operating frequency (f_{op}); then, a low-pass filter (LPF) is used to retrieve the signal component at f_{op} or its multiples [22,26]. The phase noise in high-Q

mechanical oscillators, such as QTFs, could be detrimental when LIAs are employed, since the amplitude of the output signal, and, in turn, the SNR, will be affected [27].

Both QTF signal and noise sources undergo the signal conditioning chain composed of the front-end voltage amplifier, the multiplication with a sine wave at frequency f_{op} , and the low-pass filter. Therefore, a study on the SNR as a function of (i) the parameters of the amplifier components, (ii) the operating frequency, and (iii) the low-pass filter bandwidth must be carefully conducted to fully exploit the resonance properties of the QTF and maximize the performances of a QEPAS sensor.

In this work, we reported the effect of the R_L value on the frequency where the SNR exhibits its peak at the output of the lock-in amplifier, i.e., the optimum operating frequency for the QEPAS system. Starting from the well-known Butterworth–Van Dyke model for the QTF [17,28–30], we derived an analytical expression for the amplitude of the signal generated by the QTF as a function of frequency at different R_L values. For our purposes, only the main electronic noise contributions were considered, whereas phase noise was not taken into account. Furthermore, a mathematical modelling was developed with MATLAB for all the relevant contributions to the total noise spectral density at the output of the preamplifier, making possible a comparison among their relative weights. Finally, the behavior of the SNR as a function of the lock-in demodulation frequency was studied at different R_L values and LPF bandwidths, namely, the acquisition time. All the proposed analytical expressions were validated by comparing the developed MATLAB model with SPICE simulations, carried out considering a realistic model for the OPAMP used in the preamplifier. As a result of the study, general guidelines for the choice of the resistor R_L and the most suitable operating frequency for the QEPAS system implementing the voltage-mode read-out of QTFs can be derived. Furthermore, the proposed analysis allows for the study of the noise contributions at different bandwidths to optimize the acquisition time of QEPAS measurements.

2. Signal Response of a Quartz Tuning Fork Read Out in Voltage Mode

As mentioned above, the Butterworth–Van Dyke circuit and an equivalent Thevenin source were employed to model the QTF when excited by an acoustic wave [17] to find an analytical expression of the output signal V_{out} as a function of frequency for the circuit in Figure 2. For this investigation, we considered (i) an OPAMP with sufficiently high gain-bandwidth product so that the gain of the non-inverting configuration is $A_v = V_{out}/V_{qtf} = 1 + R_F/R_S$, as shown in Figure 2; and (ii) the capacitance C_{in} between the non-inverting input and ground. Thus, the circuit to be studied is sketched in Figure 3.

Here, the parasitic shunt capacitance C_p between the terminals of the QTF is in parallel with the input capacitance of the voltage amplifier C_{in} , so that the total parasitic capacitance which loads the QTF is $C_{pt} = C_p + C_{in}$. The voltage source V_{in} represents the internal electric signal generated by the piezoelectric effect, when the QTF is excited by an acoustic wave. Straightforward calculations provide the expression of the transfer function $H_v(j\omega)$ between the internal voltage $V_{in}(j\omega)$ and the output voltage $V_{out}(j\omega)$:

$$H_v(j\omega) = \frac{V_{out}(j\omega)}{V_{in}(j\omega)} = \frac{j\omega C_s R_L}{1 - \omega^2(LC_s + R_p R_L C_{pt} C_s) + j\omega[(R_p + R_L)C_s + R_L C_{pt} - \omega^2 L C_{pt} C_s R_L]} \tag{1}$$

The squared modulus of this transfer function, which describes how the squared amplitude of the circuit response depends on the frequency, can be written as follows:

$$|H_v(j\omega)|^2 = \frac{A_v^2}{\frac{\left(1 - \frac{\omega^2}{\omega_R^2}\right)^2}{\omega^2 R_L^2 C_s^2} + \left(1 + \frac{C_{pt}}{C_s}\right)^2 \left[\left(1 - \frac{\omega^2}{\omega_p^2}\right) + \frac{R_p}{R_L} \frac{C_s}{C_{pt} + C_s}\right]^2} \tag{2}$$

where $\omega_R = \frac{1}{\sqrt{LC_s + R_p R_L C_{pt} C_s}}$ is the angular frequency in which the transfer function $H_v(j\omega)$ exhibits a real value and $\omega_P = \frac{1}{\sqrt{L \frac{C_s C_{pt}}{C_s + C_{pt}}}} = \frac{1}{\sqrt{LC_{eq}}}$ is the parallel-resonant angular frequency of the QTF as loaded in the circuit shown in Figure 3.

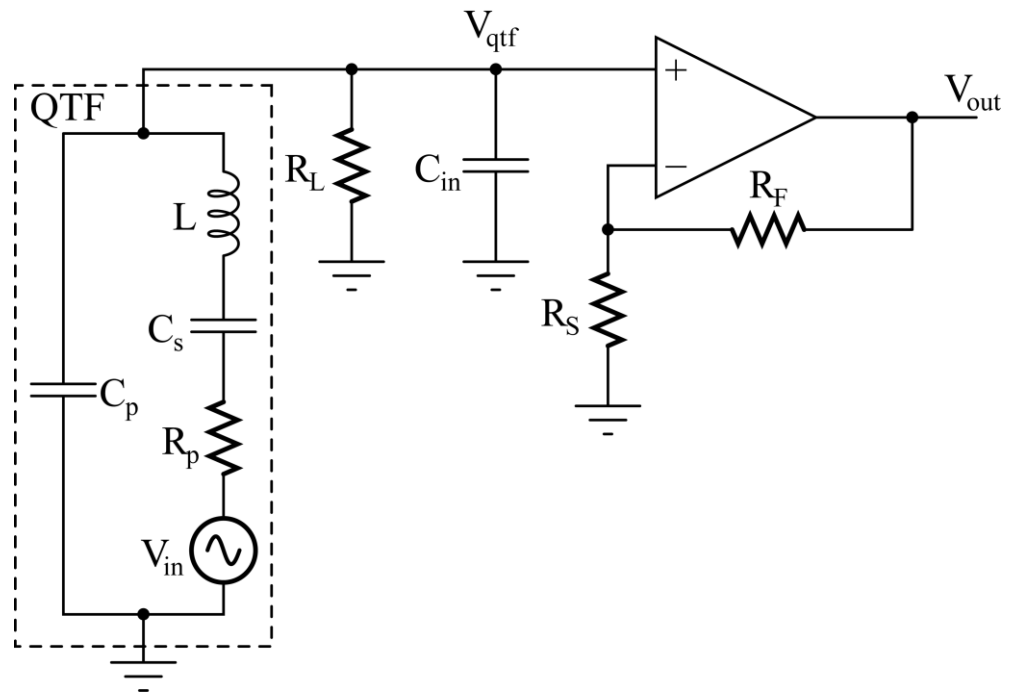


Figure 3. Butterworth–Van Dyke model for the QTF in the voltage-mode read-out circuit.

AC SPICE simulations have been carried out to confirm the validity of the expression in Equation (2). The set of typical parameters listed in Table 1 has been used for the QTF in both the analytical model and SPICE simulations. Moreover, in SPICE simulations, C_{in} is included in the model of the AD8067, provided by Analog Devices. AD8067 is a low-noise, high speed, FET input operational amplifier. Thanks to its very low input bias current, it is suitable for precision and high gain applications [31].

Table 1. Parameter values used to compare the results of expression in Equation (2) to SPICE simulations.

Parameter	Value
C_p	5 pF
C_s	5.2424 fF
L	4.5 kH
R_p	92.7 kΩ
C_{in}	1.5 pF
R_F	47 kΩ
R_S	1 kΩ

The series-resonant frequency f_s of the QTF is:

$$f_s = \frac{\omega_s}{2\pi} = \frac{1}{2\pi\sqrt{LC_s}} = 32768 \text{ Hz,}$$

whereas its quality factor Q is

$$Q = \frac{1}{\omega_s R_p C_s} = 10^4,$$

which are typical values for a standard QTF used in QEPAS sensors [2,16,17,26]. Moreover, the gain of the non-inverting configuration is $A_v = 48$ and the parallel-resonant frequency of the QTF is $f_p = \omega_p / 2\pi = 32,781$ Hz. The value of $C_p \cong C_p + C_s$ could be found by measuring the equivalent capacitance of the QTF at low frequencies using the capacitance-voltage profiling technique. The ratio C_s / C_p is extracted by the ratio f_p / f_s after measuring the parallel and series-resonant frequencies of the QTF, where the sensor exhibits the minimum and maximum admittance, respectively. Last, L can be found from f_s , knowing C_s , and R_p is extracted from the quality factor Q of the QTF [21]. Figure 4 shows the comparison between the results provided by the SPICE simulations and the analytical model for three different values of R_L (100 k Ω , 0.5 M Ω , and 2.5 M Ω).

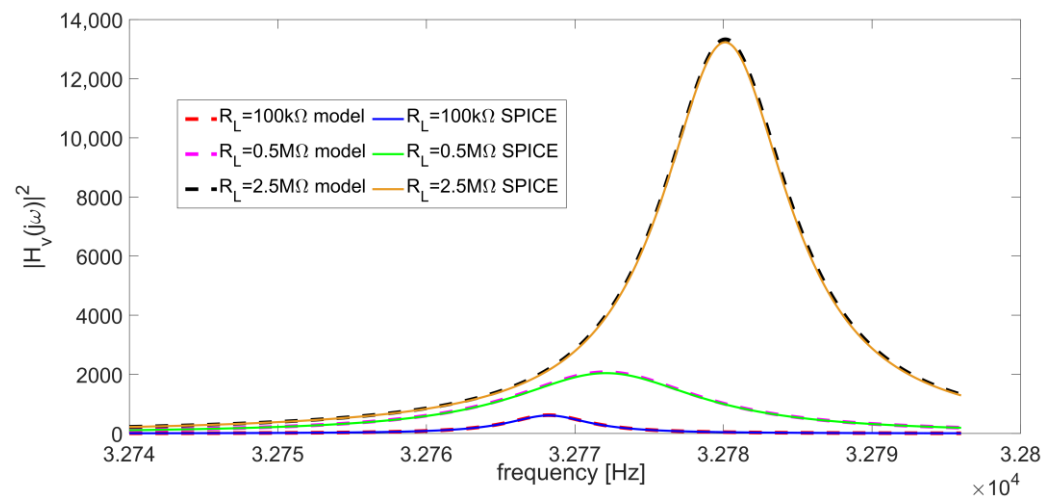


Figure 4. Comparison between SPICE simulations and analytical model in Equation (2) of the frequency response of the circuit in Figure 3 for $R_L = 100$ k Ω , 0.5 M Ω and 2.5 M Ω .

The perfect matching between two modellings demonstrates that Equation (2) can be used to accurately represent the behavior of the circuit in Figure 3. The maximum difference between the peak frequencies of corresponding curves is in the order of a few hundredths of Hz and the mean absolute percentage error between corresponding curves is about 1.8%.

2.1. Peak Frequency of the QTF Signal Response as a Function of R_L

As shown in Figure 4, the output signal amplitude and the peak frequency f_{peak} strongly depend on the value of the resistor R_L . This is particularly relevant for an optimal choice of the operating frequency in the QEPAS technique, aimed at exploiting as much as possible the resonance properties of the QTF.

Figure 5 shows the f_{peak} trend as a function of R_L . This curve was retrieved computing $|H_v(j\omega)|^2$ for different values of R_L and then applying MATLAB “max” function to yield f_{peak} values.

For R_L values lower than 100 k Ω , f_{peak} tends to the series-resonant frequency $f_s = 32768$ Hz; whereas, for values of R_L higher than 2 M Ω , f_{peak} tends to assume the values of the parallel-resonant frequency f_p , in our case equal to 32781 Hz.

The behavior of the peak position as a function of the value of R_L can be explained considering the two terms which compose the denominator of the function $|H_v(j\omega)|^2$ in Equation (2), reported here, below, for ease of reading, as Den1 and Den2:

$$Den1(\omega) = \frac{\left(1 - \frac{\omega^2}{\omega_R^2}\right)^2}{\omega^2 R_L^2 C_s^2}, \quad Den2(\omega) = \left(1 + \frac{C_{pt}}{C_s}\right)^2 \left[\left(1 - \frac{\omega^2}{\omega_p^2}\right) + \frac{R_p}{R_L} \frac{C_s}{C_{pt} + C_s} \right]^2 \quad (3)$$

The behavior of Den1 and Den2 as a function of frequency is reported in Figure 6a,b for $R_L = 100\text{ k}\Omega$ and $R_L = 10\text{ M}\Omega$, respectively.

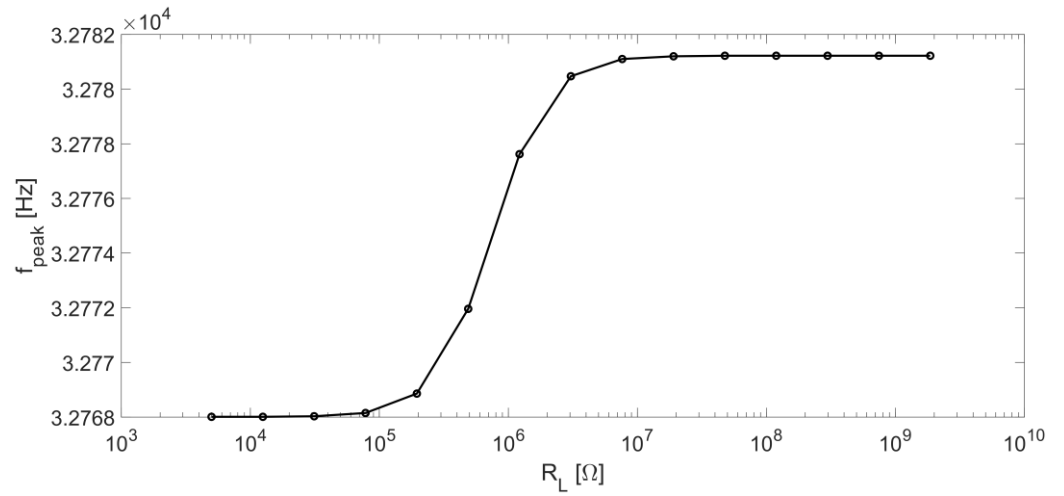


Figure 5. Peak frequency f_{peak} of $|H_v|^2$ as a function of R_L .

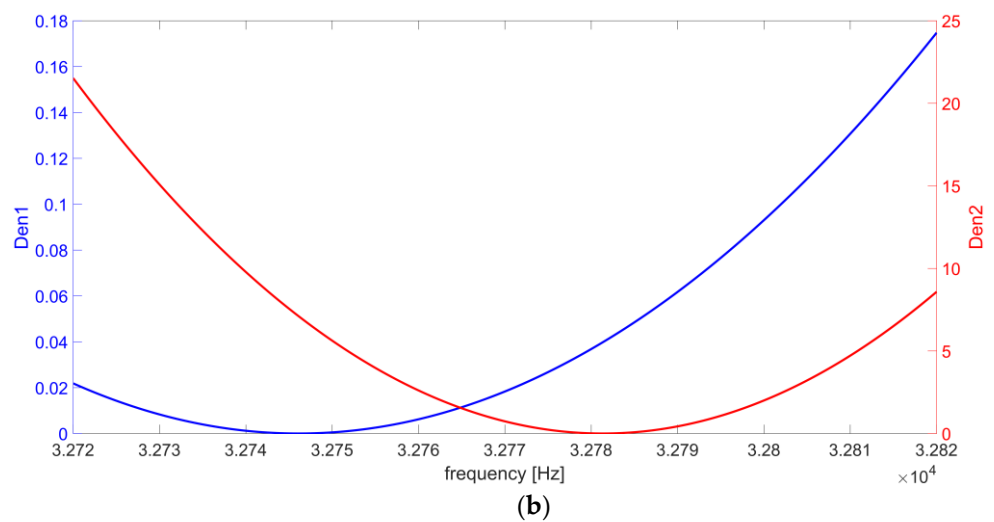
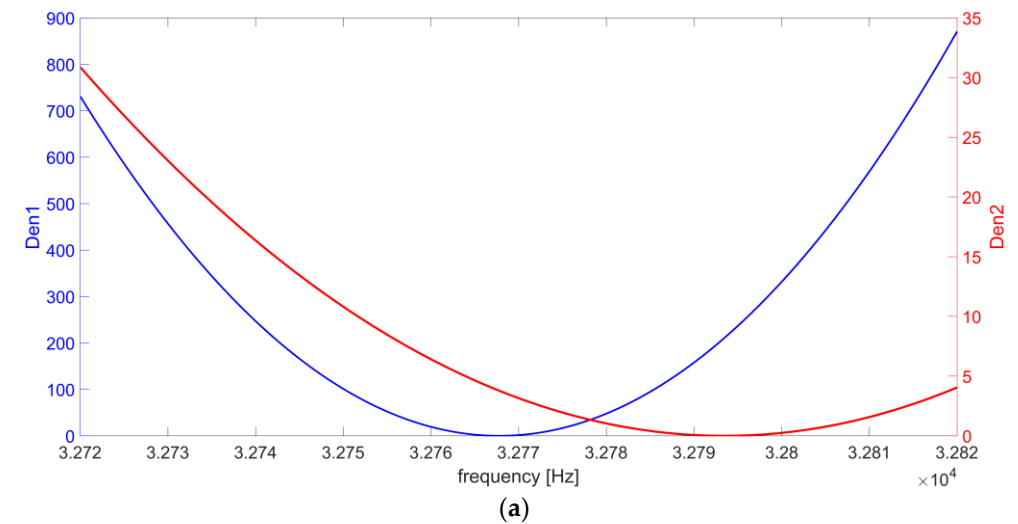


Figure 6. Behavior of Den1(f) and Den2(f) in Equation (3) as a function of frequency for (a) $R_L = 100\text{ k}\Omega$ and (b) $R_L = 10\text{ M}\Omega$.

Results show that Den1(ω) is strongly dependent on the value of R_L . In the investigated frequency range: (i) the maximum value of Den1 varies from 868.3 in Figure 6a to 0.17 in Figure 6b; (ii) the blue curve at 100 k Ω varies more rapidly than the Den1 curve at 10 M Ω in the frequency range close to the minimum; and (iii) the frequency where the Den1 minimum occurs decreases by more than 20 Hz, from 32,768 Hz in Figure 6a to 32,746 Hz in Figure 6b. Conversely, the dependence of Den2(ω) on R_L is only due to the term $\frac{R_p}{R_L} \frac{C_s}{C_{pt} + C_s}$, which is negligible when $R_L \geq 1$ M Ω , since $C_s \ll C_{pt}$ and $R_p \ll R_L$. Indeed: (i) the red curve maximum value varies from 30.8 in Figure 6a to 21.5 in Figure 6b; (ii) Den2 value variations in the frequency range close to the minimum value are slightly different at 100 k Ω and at 10 M Ω ; and (iii) the difference frequency where the Den2 minimum occurs is about 13 Hz, from 32,794 Hz in Figure 6a to 32,781 Hz in Figure 6b. As a result, for $R_L < 100$ k Ω , the contribution of Den1(ω) becomes dominant, so that when R_L decreases, the minimum value of the denominator of $|H_v(j\omega)|^2$ tends to the zero of Den1(ω) function, located at $\omega = \omega_R$. Moreover, in this range of R_L values, ω_R could be approximated to ω_S :

$$\omega_R = \frac{1}{\sqrt{LC_s + R_p R_L C_{pt} C_s}} \cong \frac{1}{\sqrt{LC_s}} = \omega_S,$$

and the peak of $|H_v(j\omega)|^2$ tends to the series-resonant frequency of the QTF. Instead, for $R_L > 2$ M Ω , Den1(ω) becomes less relevant and Den2(ω) tends to be dominant in the sum of the two terms. As a consequence, the minimum of the sum tends to the zero of Den2(ω). Finally, in this range of R_L , this zero is very close to $\omega = \omega_P$, thus, the peak of $|H_v(j\omega)|^2$ is almost coincident with the parallel-resonant frequency of the QTF.

2.2. Peak of the QTF Signal Response as a Function of R_L

The trend of the peak value of $|H_v(j\omega)|^2$ as a function of R_L value is shown in Figure 7. The same method applied for Figure 5 was used to obtain this curve.

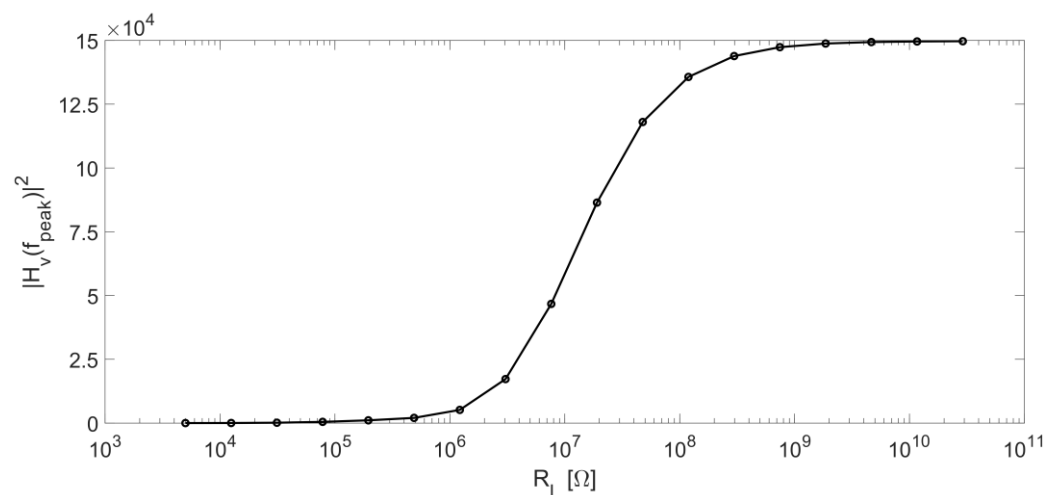


Figure 7. Peak value of $|H_v|^2$ as a function of R_L .

The peak value of $|H_v(j\omega)|^2$ is an increasing function of R_L up to a saturation value at $R_L > 1$ G Ω . As discussed in the previous section, for large values of R_L , $\omega_{peak} = 2\pi f_{peak}$ is very close to the parallel-resonant angular frequency ω_P and the peak of $|H_v(j\omega)|^2$ tends to the following value:

$$|H_v(j\omega_{peak})|^2 \cong |H_v(j\omega_P)|^2 \cong A_v^2 \frac{\omega_P^2 R_L^2 C_s^2}{\left(1 - \frac{\omega_P^2}{\omega_R^2}\right)^2} \tag{4}$$

The denominator of Equation (4) can be rewritten as:

$$1 - \frac{\omega_P^2}{\omega_R^2} = 1 - \frac{LC_s + R_p R_L C_{pt} C_s}{LC_{eq}} = \frac{L(C_{eq} - C_s) - R_p R_L C_{pt} C_s}{LC_{eq}} \cong -\frac{R_p R_L C_{pt}}{L}$$

Since $C_{Equation} \cong C_s$ and R_L is very large, it results

$$|H_v(j\omega_{peak})|^2 \cong A_v^2 \frac{\frac{1}{LC_{eq}} R_L^2 C_s^2}{\frac{R_p^2 R_L^2 C_{pt}^2}{L^2}} \cong A_v^2 \frac{LC_s}{R_p^2 C_{pt}^2},$$

which is independent on R_L .

However, the performance of the QEPAS technique will depend on the SNR obtained at the output of the preamplifier, not only on the amplitude of the signal. Therefore, it is mandatory to carry out a detailed study of the electronic noise contributions that are involved in the circuit, with the purpose of finding out the optimal operating frequency maximizing the SNR.

3. Contributions to the Output Noise Spectral Density

The most relevant contributions to the total electronic noise at the output of the voltage-mode preamplifier are shown in Figure 8.

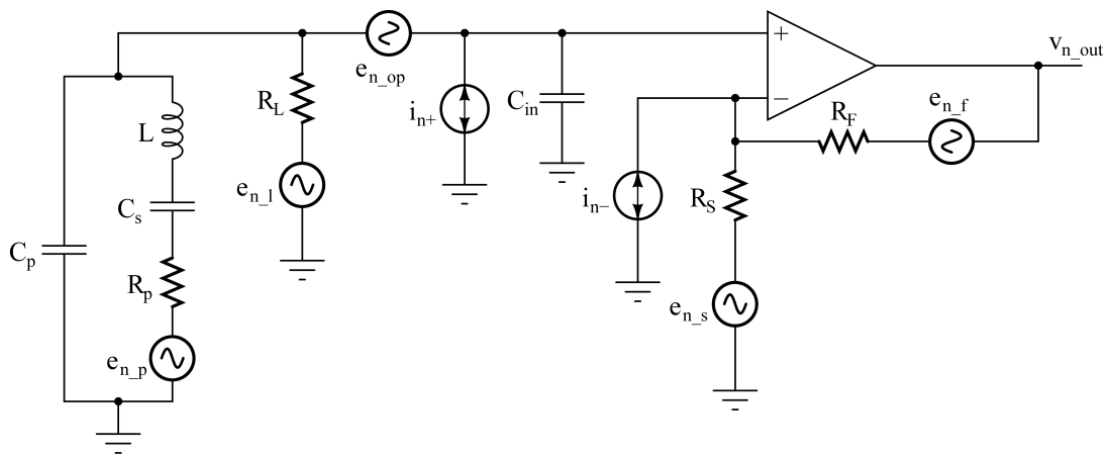


Figure 8. Noise contributions in the circuit of Figure 3.

In our calculation, the phase noise was neglected [27] and only the main electronic noise contributions were considered. Each resistor R_i of the circuit has been associated to its thermal noise voltage source, $e_{n_i}^2 = 4kTR_i$. The OPAMP noise has been characterized by means of the classic equivalent input noise voltage (e_{n_op}) and current (i_{n+} and i_{n-}) sources. To simplify the study without losing accuracy, it is possible to neglect the noise contributions of R_f and R_s , composing the feedback network, due to the small values of these resistors. For the same reasons, the equivalent noise current i_{n-} associated to the inverting input of the OPAMP likewise does not give any relevant contribution. Moreover, all the sources in Figure 8 can be considered independent, so that the total output noise power spectral density $S_{ntot}(\omega)$ can be evaluated as follows:

$$S_{ntot}(\omega) \cong S_{np}(\omega) + S_{nL}(\omega) + S_{nop}(\omega) + S_{nin+}(\omega), \tag{5}$$

where the terms of the right-hand side come from R_p , R_L , e_{n_op} , and i_{n+} , respectively. In Equation (5), the single terms are the product of the spectral density of each noise source multiplied by the squared modulus of the transfer function between the noise source and the output of the circuit, determined using the superposition principle [32].

Concerning the noise associated to the resistor R_p , the transfer function $S_{np}(\omega)$ between the source e_{n_p} and the output of the preamplifier is $H_v(j\omega)$, thus:

$$S_{np}(\omega) = 4kTR_p |H_v(j\omega)|^2.$$

As a consequence, the behavior of $S_{np}(\omega)$ as a function of both the frequency and R_L is the same discussed in Section 2.

Let us now consider the noise contribution from the resistor R_L . The transfer function between the source e_{n_l} and the output of the front-end is:

$$H_L(j\omega) = \frac{V_{n_out}(j\omega)}{e_{n_l}(j\omega)} = A_v \frac{1 - \omega^2 LC_s + j\omega R_p C_s}{1 - \frac{\omega^2}{\omega_R^2} + j\omega [(R_L + R_p)C_s + R_L C_{pt} - \omega^2 LC_{pt} C_s R_L]} \quad (6)$$

The denominators of $H_v(j\omega)$ and $H_L(j\omega)$ are the same and the two transfer functions differ only in their numerator. The contribution of the thermal noise of the resistor R_L to the total output noise spectral density is:

$$S_{nL}(\omega) = 4kTR_L |H_L(j\omega)|^2. \quad (7)$$

Figure 9 shows the behavior of S_{nL} as a function of the frequency, for four different values of R_L (100 k Ω , 500 k Ω , 6 M Ω , and 20 M Ω).

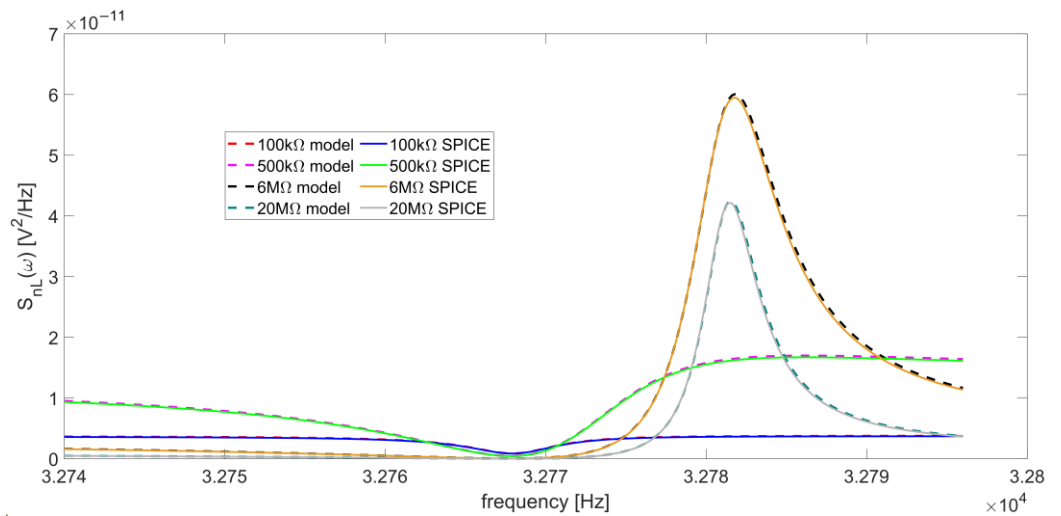


Figure 9. Comparison between SPICE simulations and analytical model described in Equation (7) of the output noise spectral density contribution from the thermal noise of R_L , for four different values of the resistor: 100 k Ω , 500 k Ω , 6 M Ω , and 20 M Ω .

The curves calculated with Equation (7) and those obtained by SPICE simulation are in excellent agreement. The function $|H_L(j\omega)|$ has a minimum located at $\omega = \omega_S$, since, at the series-resonant frequency, the Butterworth–Van Dyke impedance model of the QTF is reduced to R_p , which is its minimum value. Accordingly, also $S_{nL}(\omega)$ exhibits a minimum at the same frequency. Furthermore, a peak appears around the parallel-resonant frequency for increasing values of R_L . Figure 10 reports the behavior of the peak value of $S_{nL}(\omega)$ as a function of R_L , which varies from 500 k Ω to 20 M Ω .

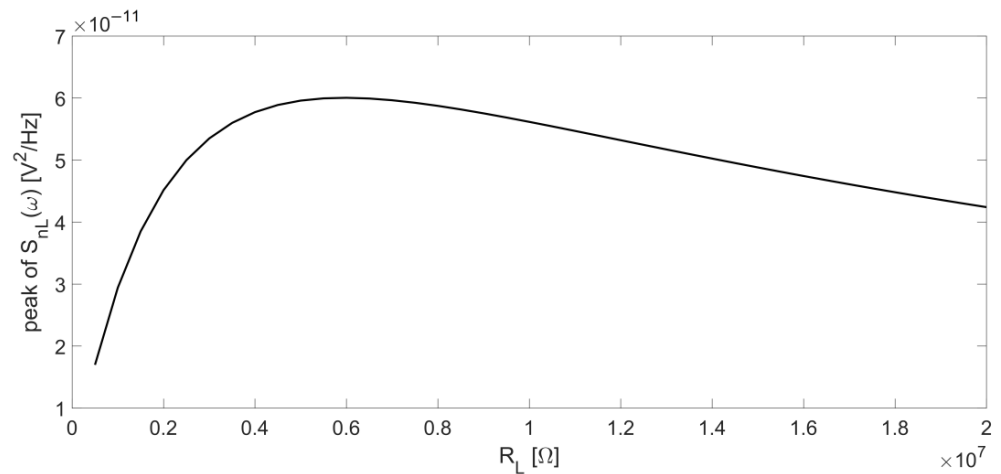


Figure 10. Peak of the output noise spectral density contribution due to R_L as a function of R_L itself.

Using the set of parameters listed in Table 1, starting from low values of R_L , this peak appears when $R_L \cong 500 \text{ k}\Omega$ (dashed magenta and green curves in Figure 9), then increases up to $R_L \cong 6 \text{ M}\Omega$ (Figure 10). Beyond this value, the peak decreases for increasing values of R_L and the function $S_{nL}(\omega)$ assumes lower values in the frequency range under investigation.

Figures 7 and 10 suggest that, at least for what concerns the noise contributions considered up to now, it is convenient to work with large values of the resistor R_L because the amplitude of the output signal increases with R_L (see Figure 7) and the noise contribution due to this resistor decreases (see Figure 10), whereas the contribution from the thermal noise of R_p has exactly the same frequency behavior of the signal.

Let us now consider the contribution of the input equivalent voltage noise of the OPAMP to the total output noise:

$$S_{nop}(\omega) = e_{n_{op}}^2 |H_{en}(j\omega)|^2. \tag{8}$$

Since the flicker noise has been considered negligible in the narrow bandwidth of interest, namely, around the QTF resonance frequency, the input equivalent noise voltage has a constant power spectral density, i.e., it can be considered as white noise. The value of $e_{n_{op}}$ has been set at $6.6 \text{ nV}/\sqrt{\text{Hz}}$, as reported in the data sheet of the AD8067 [31]. The transfer function $H_{en}(j\omega)$ is the following:

$$\begin{aligned} H_{en}(j\omega) &= \frac{V_{n_{out}}(j\omega)}{e_{n_{op}}(j\omega)} \\ &= A_v \frac{1 - \omega^2(LC_s + R_p R_L C_p C_s) + j\omega[(R_p + R_L)C_s + R_L C_p - \omega^2 L C_p C_s R_L]}{1 - \omega^2(LC_s + R_p R_L C_{pt} C_s) + j\omega[(R_p + R_L)C_s + R_L C_{pt} - \omega^2 L C_{pt} C_s R_L]}, \end{aligned} \tag{9}$$

in which the numerator differs from the denominator only for the capacitance $C_{pt} = C_p + C_{in}$ replaced by C_p . This contribution can be considered as constant in the frequency range investigated for QEPAS applications.

The contribution of the input equivalent current noise i_{n+} to the overall output noise spectral density $S_{ntot}(\omega)$ is

$$S_{nin+}(\omega) = i_{n+}^2(\omega) R_L^2 |H_L(j\omega)|^2. \tag{10}$$

Using Equations (10) and (7), the contributions to $S_{ntot}(\omega)$, respectively due to i_{n+} and R_L , can be compared:

$$\frac{S_{nin+}(\omega)}{S_{nL}(\omega)} = \frac{i_{n+}^2(\omega) R_L}{4kT}.$$

The contribution of $S_{in+}(\omega)$ can be neglected with respect to $S_{nL}(\omega)$ if

$$i_{n+}^2(\omega) \ll \frac{4kT}{R_L}.$$

If we consider a large R_L value, i.e., 100 M Ω , $S_{in+}(\omega)$ will be negligible at room temperature if $i_{n+} \ll 13$ fA/ $\sqrt{\text{Hz}}$. Since the AD8067 has FET inputs, $i_{n+}(\omega)$ cannot be considered white, but is a linear function of the frequency, in the range where the flicker noise can be neglected [33]. In our model, the value of $i_{n+}(\omega)$ at 10 kHz has been set to 1 fA/ $\sqrt{\text{Hz}}$, a slightly higher value than the one reported in the datasheet of the OPAMP, which is 0.6 fA/ $\sqrt{\text{Hz}}$ [31], and the slope of the linear function has been set to +20 dB/dec [33]. Figure 11 shows the excellent correspondence between the analytical model used for $i_{n+}(\omega)$ and the input equivalent noise current resulting from a simulation carried out with the SPICE model of the AD8067.

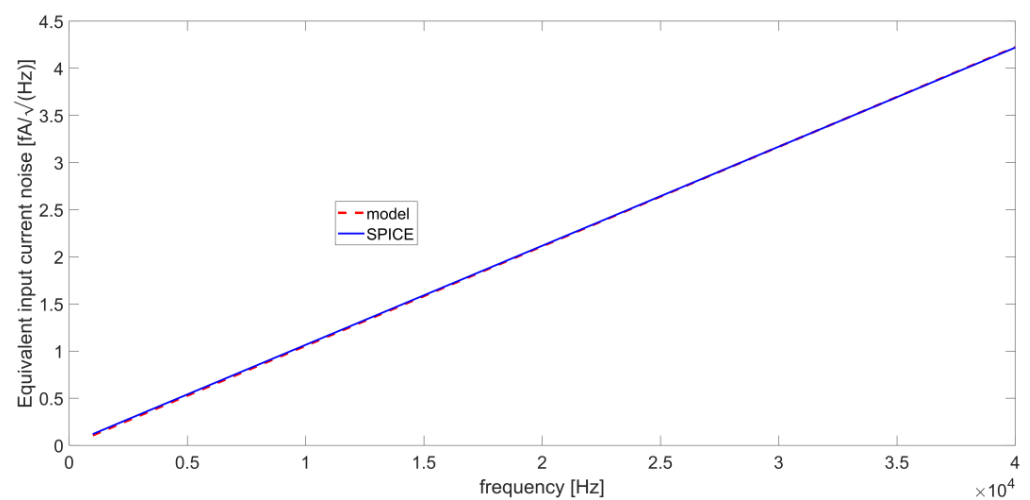
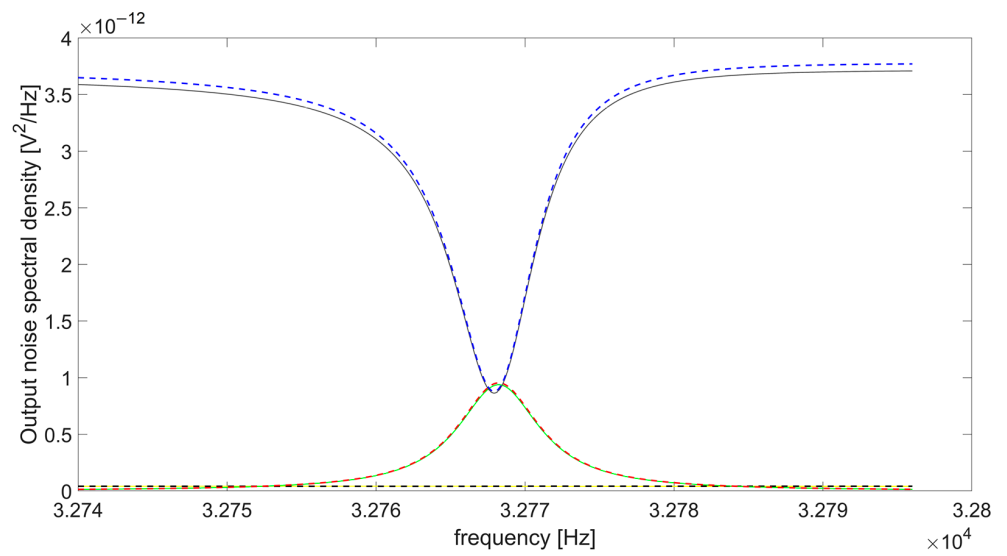


Figure 11. Fitting between the analytical model and SPICE simulations of the input equivalent noise current of the AD8067.

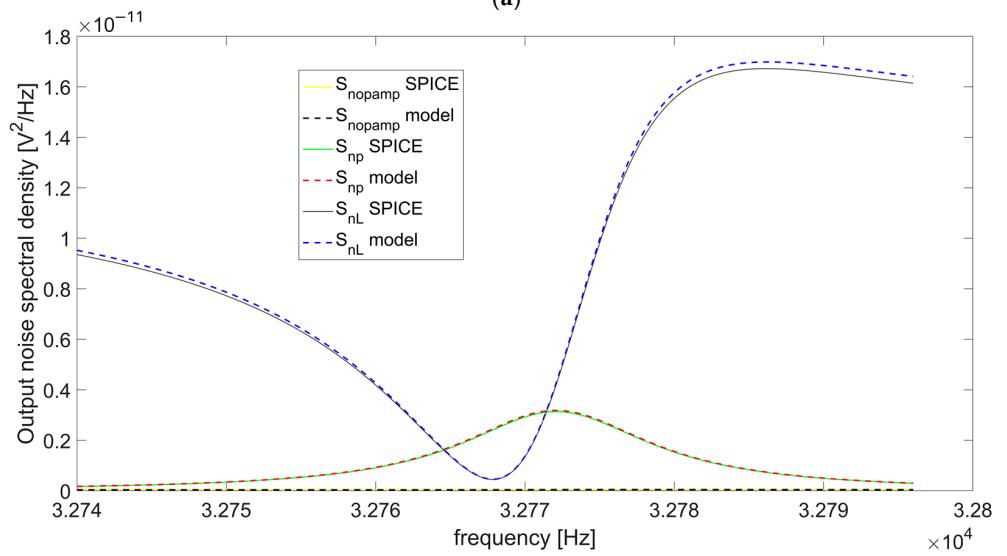
It is worth noticing that around the resonance frequencies of the QTF, the level of $i_{n+}(\omega)$ remains lower than the limit of 13 fA/ $\sqrt{\text{Hz}}$ determined above. Thus, we can conclude that the contribution $S_{in+}(\omega)$ can be neglected with respect to $S_{nL}(\omega)$ in the noise analysis of our circuit without losing accuracy.

The analysis carried out so far allows for a comparison of the terms in Equation (5) to understand which ones are dominant for the output noise spectral density of the preamplifier. Figure 12 compares the spectral contributions of the OPAMP and the resistors R_p and R_L to the overall $S_{ntot}(\omega)$ at the output of the circuit. The terms due to $e_{n_{op}}$ and i_{n+} , namely, $S_{nop}(\omega)$ and $S_{nin+}(\omega)$, respectively, have been summed, resulting in the overall noise contribution of the OPAMP ($S_{opamp}(\omega)$) and allowing for a comparison of the analytical model with the results of SPICE simulations, in which the two terms are not distinguishable. The same R_L values of Figure 9 have been considered (100 k Ω , 500 k Ω , 6 M Ω , and 20 M Ω).

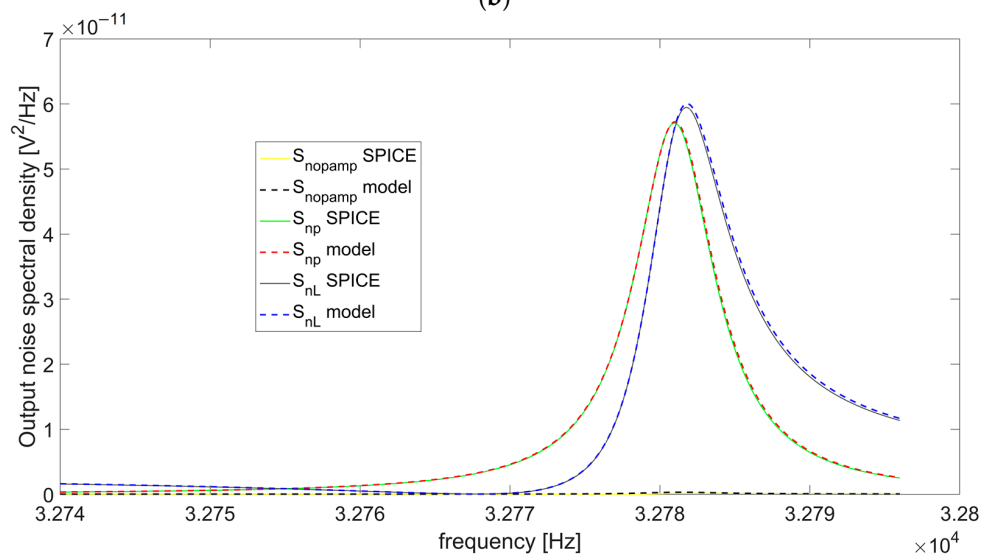
For all the considered cases, the results provided by the analytical model and the SPICE simulations exhibit a very good agreement. In addition, the contribution of the OPAMP to the total output noise is always negligible compared to the sum of the contributions from R_L and R_p . $S_{nL}(\omega)$ tends to prevail over $S_{np}(\omega)$ for $R_L < 6$ M Ω (Figure 12a,b), whereas the opposite happens when the value of R_L is larger than 6 M Ω (Figure 12c,d). This confirms the previous conclusion about the advantage of working with large values of the resistor R_L in order to achieve good performance in terms of SNR.



(a)



(b)



(c)

Figure 12. Cont.

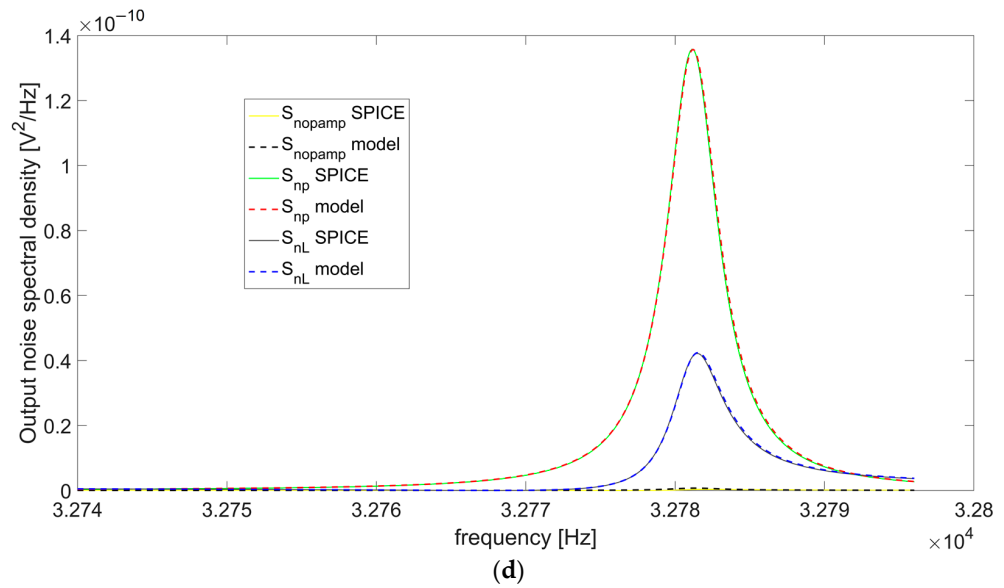


Figure 12. Contributions to the overall output noise spectral density due to the OPAMP and resistors R_p and R_L , for (a) $R_L = 100 \text{ k}\Omega$, (b) $R_L = 500 \text{ k}\Omega$, (c) $R_L = 6 \text{ M}\Omega$, (d) $R_L = 20 \text{ M}\Omega$: comparison between the results obtained with the analytical model and SPICE simulations.

4. Signal-to-Noise Ratio at the Output of the Lock-in Amplifier

Synchronous detection techniques based on laser modulation and lock-in amplifier are always used in QEPAS sensors to increase the SNR of the measurements. In the previous sections, the amplitude of the useful signal and the noise spectral density at the output of the voltage-mode preamplifier are expressed as a function of frequency. These expressions can be conveniently exploited to evaluate the SNR at the output of the LIA. Thanks to synchronous demodulation and narrow-band low-pass filtering, the LIA output signal is DC-level proportional to the amplitude of the preamplifier response at the operating frequency. When the preamplifier response is acquired at the QTF resonance frequency, the trend of the SNR can be investigated in a small range around f_s . Thus, if the preamplifier response is acquired at a certain frequency f_{op} close to f_s , the output signal is proportional to $|H_v(f_{op})|$. For what concerns noise, as a result of demodulation, the LIA transfers around DC the noise spectrum at the output of the preamplifier, centered around the LIA reference frequency. This noise is then filtered by means of the LIA narrow low-pass filter. Thus, the LIA behaves in practice like a narrow band-pass filter centered around its reference frequency. Hence, LIA was modelled as a biquadratic band-pass filter with a transfer function:

$$H_{LIA}(j\omega) = \frac{j \frac{\omega_{op}}{Q_{filt}} \omega}{\omega_{op}^2 - \omega^2 + j \frac{\omega_{op}}{Q_{filt}} \omega}, \tag{11}$$

characterized by unity gain at center frequency and -3dB bandwidth $BW = \omega_{op}/Q_{filt}$ [34].

Therefore, we can describe the behavior of the SNR at the output of the LIA as a function of the chosen operating frequency $f_{op} = \omega_{op}/2\pi$ by means of the following function:

$$\begin{aligned} SNR_n(\omega_{op}) &= \frac{|H_v(\omega_{op})|}{\sqrt{\int_{-\infty}^{\infty} S_{ntot}(\omega) |H_{LIA}(j\omega)|^2 d\omega}} = \\ &\cong \frac{|H_v(\omega_{op})|}{\sqrt{\int_{-\infty}^{\infty} S_{np}(\omega) |H_{LIA}(j\omega)|^2 df + \int_{-\infty}^{\infty} S_{nL}(\omega) |H_{LIA}(j\omega)|^2 d\omega}} \end{aligned} \tag{12}$$

where the amplitude of the input signal V_{in} (see Figure 3) has been normalized to 1 V.

By separating the noise contributions from R_p and R_L , we can define two functions:

$$SNR_{np}^2(\omega_{op}) = \frac{|H_v(\omega_{op})|^2}{\int_{-\infty}^{\infty} S_{np}(\omega) |H_{LIA}(j\omega)|^2 d\omega}$$

and

$$SNR_{nL}^2(\omega_{op}) = \frac{|H_v(\omega_{op})|^2}{\int_{-\infty}^{\infty} S_{nL}(\omega) |H_{LIA}(j\omega)|^2 d\omega}$$

Thus, the total normalized squared-SNR can be rewritten as follows:

$$SNR_n^2 = \frac{1}{\frac{1}{SNR_{np}^2} + \frac{1}{SNR_{nL}^2}} \tag{13}$$

First, let us consider a very narrow-bandwidth $BW = 0.5$ Hz, corresponding to a settling time of about 1.3 s for an equivalent first-order LIA low-pass filter. In this case, the behavior of the integrated noise as a function of f_{op} is expected to be very similar to the output noise spectral density. Thus, the SNR_{np} contribution is expected to be almost spectrally flat since the noise from R_p and the signal have the same transfer function $H_v(f)$. Nonetheless, considering a representative value for $R_L = 100$ k Ω , a peak of SNR_{np} emerges around the peak frequency of $|H_v(f)|$, because of the effect of integration, as reported in Figure 13. As shown in Figure 13, for a bandpass filter, the effect of the integration bandwidth on the input noise spectral density can be more intuitively represented by means of a simple brick-wall filter.

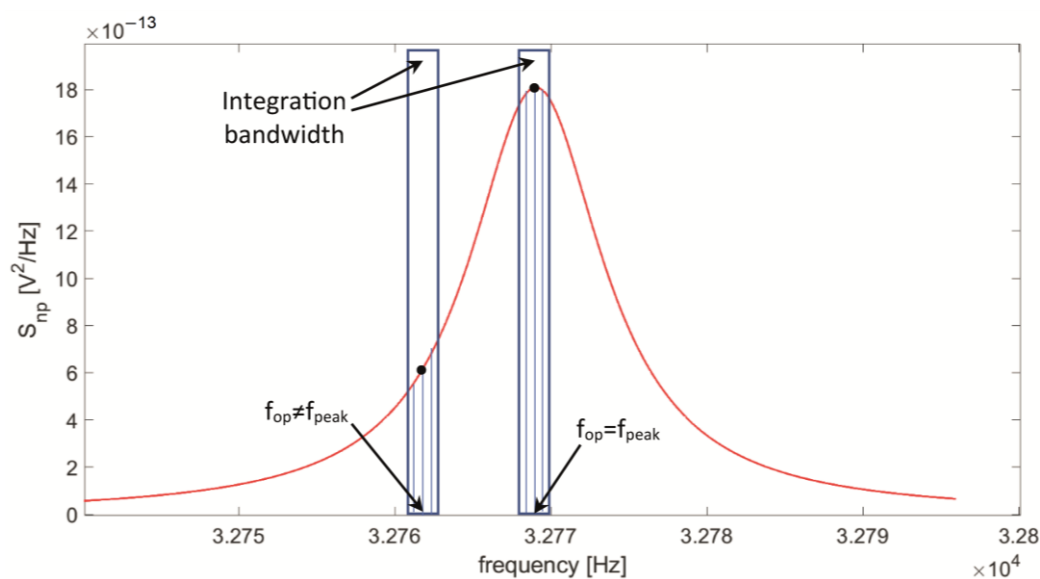


Figure 13. Integration of the contribution S_{np} (red line), due to R_p , to the total output spectral noise density at a low-pass filter bandwidth of 0.5 Hz around the operating frequency f_{op} , for $f_{op} = f_{peak}$ and $f_{op} \neq f_{peak}$ ($R_L = 100$ k Ω).

Indeed, in the narrow integration bandwidth, the function $S_{np}(f)$ takes monotonically decreasing values on both sides of $f_{op} = f_{peak}$; whereas, for any other frequency value, $S_{np}(f)$ has decreasing values in one direction, but increasing values in the other, as illustrated in Figure 13. As a consequence, the value of the integrated noise normalized to the value of the signal reaches a minimum value at $f_{op} = f_{peak}$, generating a peak value in the function $SNR_{np}(f_{op})$.

The presence of a peak value for SNR_{np} is also visible in Figure 14, which reports SNR_{np} as a function of the frequency f_{op} , for different values of R_L . Moreover, for increasing

values of R_L , the peak moves from f_S to f_P ; for large values of R_L , it becomes slightly more pronounced, even though the overall behavior always remains rather flat.

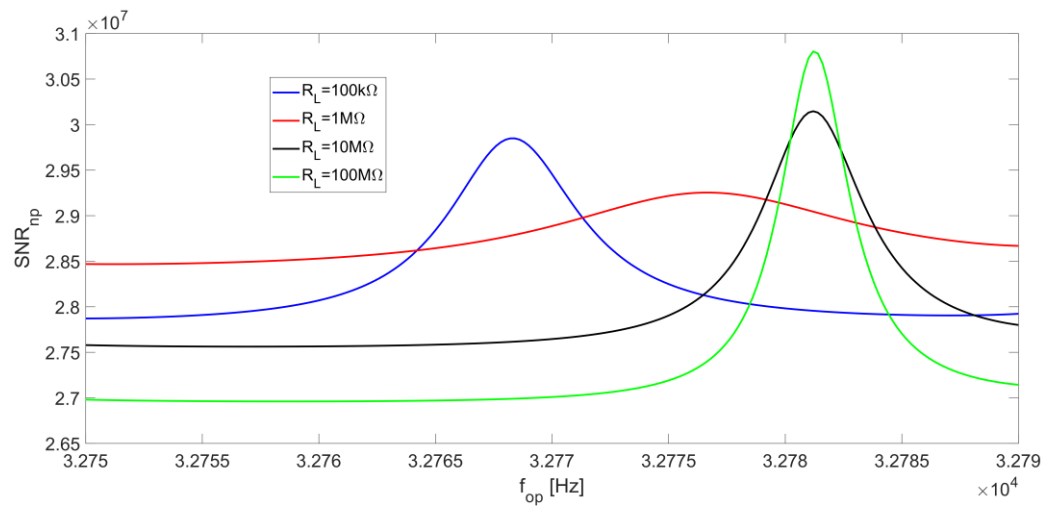


Figure 14. R_p noise contribution to the SNR_n at the LIA output as a function of the operating frequency, for different values of R_L and at a low-pass filter bandwidth of $BW = 0.5$ Hz.

As for the term SNR_{nL} , its behavior as a function of f_{op} is strongly affected by the minimum of the noise spectral density S_{nL} at f_S . This effect prevails over the peak value of the signal, which moves towards f_P for increasing values of R_L , resulting in a local maximum point on SNR_{nL} which is always located at the series-resonant frequency f_S for any value of R_L . Figure 15 shows the behavior of SNR_{nL} as a function of the operating frequency for different R_L values.

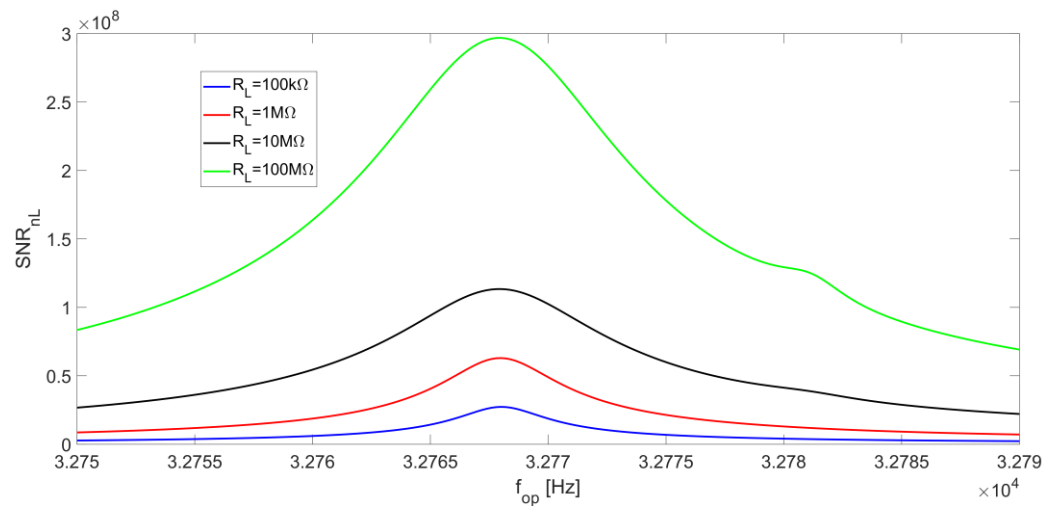


Figure 15. R_L noise contribution to the SNR_n at the LIA output as a function of the operating frequency, for different values of R_L and at a low-pass filter bandwidth of $BW = 0.5$ Hz.

Higher values of SNR_{nL} are obtained for increasing values of R_L values. Therefore, as reported in Equation (13), SNR_{np} becomes dominant in the calculation of the overall SNR for large values of R_L .

We can now consider the overall SNR at the LIA output given by Equation (13) as a function of f_{op} . Figure 16 reports the SNR_n as a function of f_{op} for different values of R_L with $BW = 0.5$ Hz. Here, a comparison between the results given by the analytical model and the corresponding SPICE simulation is also proposed, highlighting an excellent correspondence.

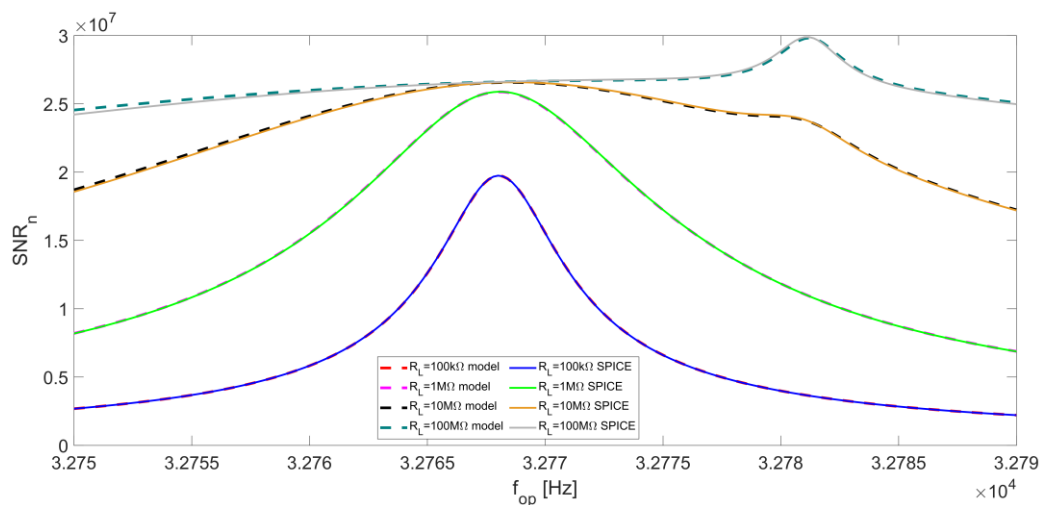


Figure 16. Total normalized signal-to-noise ratio SNR_n at the LIA output as a function of the operating frequency, for different values of R_L and at a low-pass filter bandwidth of $BW = 0.5$ Hz. The corresponding results of SPICE simulations are also reported.

For low values of R_L , SNR_{np} is almost flat (see Figure 14) and the peak of the total SNR_n coincides with the peak of SNR_{nL} , so the best operating frequency for QEPAS is the series-resonant frequency f_s of the QTF. When R_L is increased, as already pointed out, the contribution of SNR_{nL} becomes less relevant, so a local peak in the SNR_n emerges, corresponding to the peak of SNR_{np} , which occurs at the parallel-resonant frequency f_p .

From Figure 16, it is evident that the SNR_n peak feature at f_s becomes less sharp as R_L increases. For $R_L = 100$ M Ω , the SNR_n becomes quite flat around f_s and a sharp peak appears at f_p . In general, slightly better results in terms of SNR are obtained with large values of R_L .

The study above has been carried out for a LIA with a very narrow-band filter, which is useful when the requirements in terms of noise rejection are very harsh and the long time needed for a single measurement can be tolerated. With fast measurements [35,36], the bandwidth of the LIA filter must necessarily be increased, and the results of the previous analysis must be revised. Moreover, the QTF response time represents a further issue to deal with when fast measurements are needed. The response time is given by:

$$\tau = \frac{Q}{\pi f_s} \cong 100 \text{ ms.}$$

This implies that, in conventional QEPAS applications, a long integration time (300 to 400 ms) is required to acquire the LIA output signal. Nevertheless, specific QEPAS techniques such as Beat Frequency (BF) QEPAS exploit the fast transient response of an acoustically excited QTF to retrieve the gas concentration, the resonance frequency, and the quality factor of the QTF [7]. This approach overcomes the limitations imposed by the time response of the QTF, allowing shorter acquisition times and faster measurements.

As concerns the contribution to the total SNR at the LIA output due to the resistor R_p , since the integration bandwidth is larger, the effect of the integration around f_{peak} , described above (see Figure 13), is more relevant. Consequently, the peak of SNR_{np} as a function of the operating frequency, always placed at f_{peak} , becomes sharper and more pronounced. Figure 17 shows the behavior of SNR_{np} as a function of f_{op} when $BW = 5$ Hz, corresponding to a settling time of about 130 ms for an equivalent first order LIA low-pass filter for the same values of R_L considered in Figure 14.

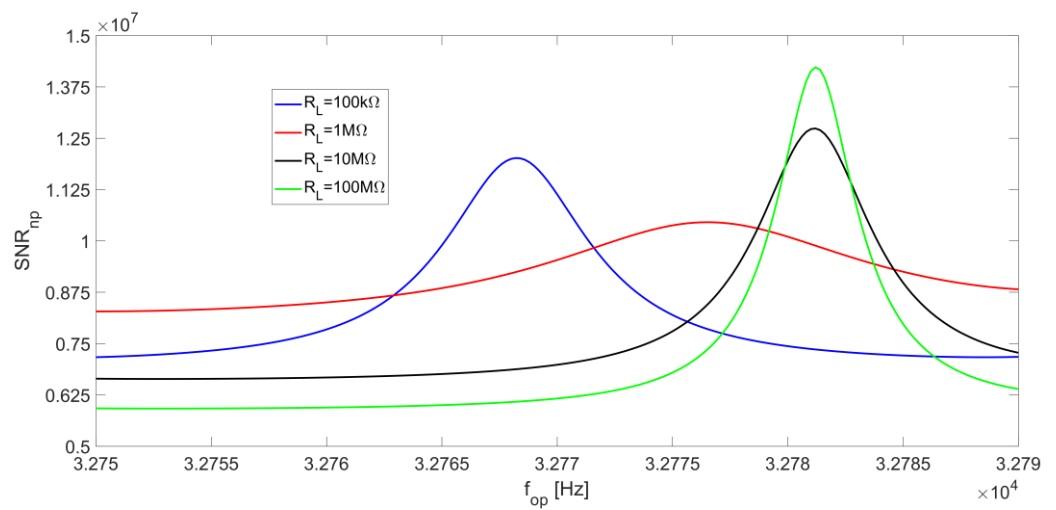


Figure 17. R_P noise contribution to the SNR_n at the LIA output as a function of the operating frequency, for different values of R_L and at a low-pass filter bandwidth of $BW = 5$ Hz.

We now analyze the R_L noise contribution to the SNR for increasing values of the LIA bandwidth. The effect of the minimum of S_{nL} , placed at f_S , tends to be less relevant, because of the increase of the integration bandwidth. Therefore, the function SNR_{nL} becomes flatter around the series-resonant frequency. Nonetheless, for small values of R_L , the peak of the signal is located at f_S and, consequently, the peak of SNR_{nL} is still placed at f_S . When R_L is increased, the peak of the signal moves towards the parallel-resonant frequency f_P and the effect of the minimum of S_{nL} becomes less relevant, so SNR_{nL} tends to be flat. For large values of R_L , S_{nL} values decrease (see Figure 12c,d), whereas the peak of the signal placed at f_P increases; as a result, SNR_{nL} exhibits a peak at f_P , which becomes sharper as R_L increases. The behavior of SNR_{nL} as a function of the operating frequency f_{op} is shown in Figure 18 for $BW = 5$ Hz.

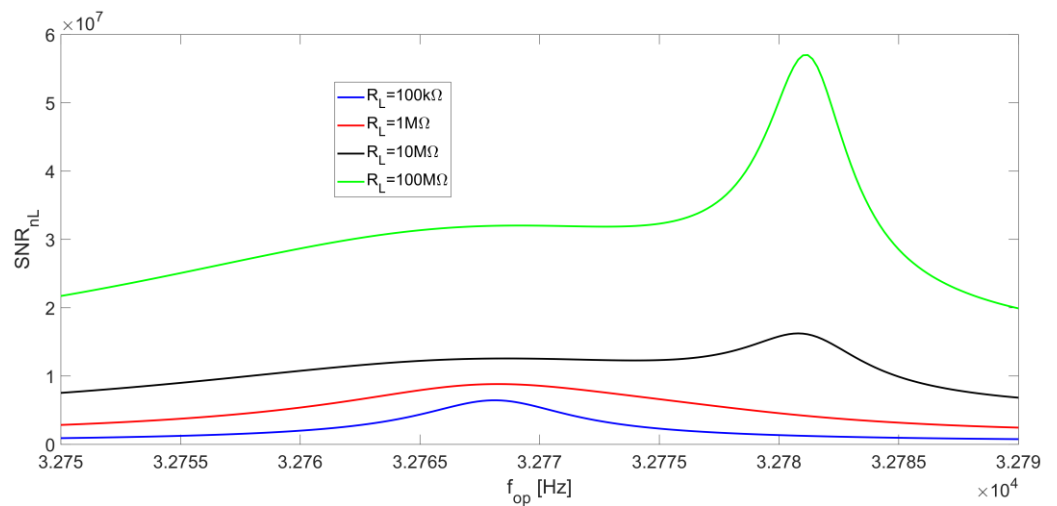


Figure 18. R_L noise contribution to the SNR_n at the LIA output as a function of the operating frequency, for different values of R_L and at a low-pass filter bandwidth of $BW = 5$ Hz.

Finally, from Equation (13), Figure 19 shows that the peak value of SNR_n results at f_S , where the peak of both SNR_{np} and SNR_{nL} is located, for low values of R_L .

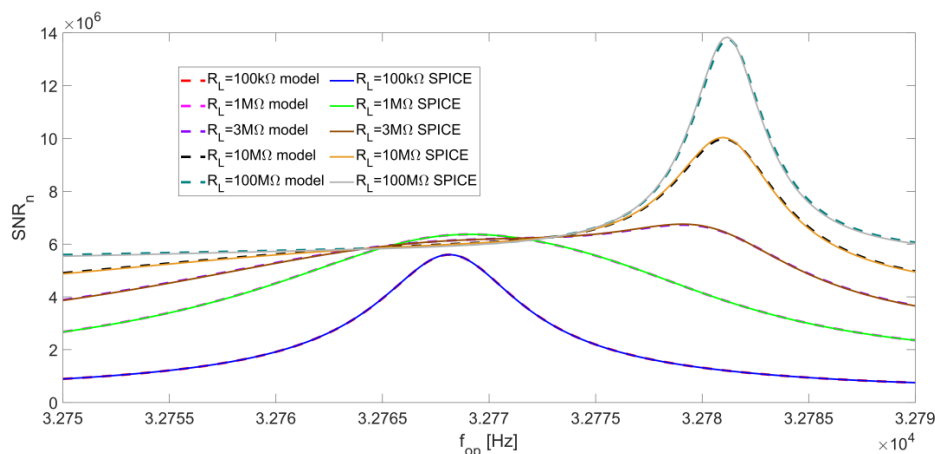


Figure 19. Total normalized signal-to-noise ratio SNR_n at the LIA output as a function of the operating frequency, for different values of R_L and at a low-pass filter bandwidth of $BW = 5$ Hz. The corresponding results of SPICE simulations are also reported.

For increasing values of R_L , the SNR_n peak feature starts to flatten out until, for values of R_L larger than about $2\text{ M}\Omega$, a peak emerges close to f_p , where both SNR_{np} and SNR_{nL} have their maximum value. This peak becomes as sharper as R_L increases, as shown in Figure 19, which represents the behavior of SNR as a function of f_{op} for $BW = 5$ Hz. Additionally in this case, SPICE simulations are in very good agreement with the results provided by the analytical model. The SNR_n peak at $100\text{ M}\Omega$ is more than two times higher than the values close to f_s .

Finally, the presented study can be applied to compute the Normalized Noise Equivalent Absorption (NNEA), an important parameter to compare QEPAS sensors [2,4,5,7,10]. NNEA is defined as follows:

$$NNEA = \frac{P \cdot \alpha}{SNR \cdot \sqrt{\Delta f}}$$

where P is the laser optical power, α is the absorption coefficient of the gas under investigation, SNR is the signal-to-noise ratio, and Δf is the integration bandwidth.

In [10], an NNEA of $5.0 \times 10^{-9}\text{ W}\cdot\text{cm}^{-1}/\sqrt{\text{Hz}}$ for the detection of CO_2 in an N_2 mixture, employing a transimpedance amplifier with a $10\text{-M}\Omega$ feedback resistor and a narrow-bandwidth LIA filter, was demonstrated. Assuming the same value of NNEA for a voltage preamplifier with a $10\text{-M}\Omega$ bias resistor and an integration bandwidth of 0.5 Hz , a $100\text{-M}\Omega$ bias resistor and the same integration bandwidth would lead to an NNEA of $4.4 \times 10^{-9}\text{ W}\cdot\text{cm}^{-1}/\sqrt{\text{Hz}}$, thus an improvement of a factor of 1.1, as suggested from Figure 16.

Considering a 5 Hz LIA filter bandwidth, an NNEA of $5.8 \times 10^{-9}\text{ W}\cdot\text{cm}^{-1}/\sqrt{\text{Hz}}$ can be calculated for a bias resistor of $10\text{ M}\Omega$. An improvement of a 1.4 factor can be calculated when a bias resistor of $100\text{ M}\Omega$ is employed, leading to a NNEA of $4.1 \times 10^{-9}\text{ W}\cdot\text{cm}^{-1}/\sqrt{\text{Hz}}$. Table 2 summarizes the NNEA values obtained for different values of R_L and Δf : it can be observed that increasing R_L at a fixed filter bandwidth always results in an improvement of the NNEA.

Table 2. NNEA for different values of R_L and Δf , calculated starting from the value reported in [10] for the detection of CO_2 in an N_2 mixture.

R_L [MΩ]	Δf [Hz]	NNEA [$\text{W}\cdot\text{cm}^{-1}/\sqrt{\text{Hz}}$]
10	0.5	5.0×10^{-9} [10]
100	0.5	4.4×10^{-9}
10	5	5.8×10^{-9}
100	5	4.1×10^{-9}

5. Discussion and Conclusions

In this work, we investigated the SNR trend as a function of the operating frequency for a voltage-mode read-out of QTFs, comparing the results obtained by the developed model with SPICE simulations. The effects of the R_L values, the operating frequency, and the bandwidth of the LIA low-pass filter on the overall SNR were investigated. We firstly demonstrated that the contribution of the OPAMP to the output noise of the voltage preamplifier can be always neglected and the output noise power density is dominated by the contributions of the QTF-equivalent resistor R_p and R_L . Moreover, the dominant contribution to the total noise changes from R_L , when $R_L < 10 \text{ M}\Omega$, to R_p , for $R_L > 10 \text{ M}\Omega$.

According to our model, the peak value of the SNR tends to increase along with the bias resistor R_L .

When a narrowband low-pass filter of the LIA is employed (e.g., bandwidth of 0.5 Hz), the curves shown in Figure 16 suggest that only a limited increase of the SNR can be obtained by either increasing the value of the resistor R_L or varying the operating frequency. For $R_L < 10 \text{ M}\Omega$, the best operating frequency for the QEPAS technique is the series-resonant frequency of the QTF f_s , where SNR function exhibits a peak value. This peak becomes less pronounced when R_L is increased. A 10-M Ω bias resistor ensures a 1.3 times higher SNR at the series-resonant frequency f_s , with respect to a 100 k Ω -bias resistor. For large values of R_L , SNR tends to be flat around f_s and a small peak emerges at the parallel-resonant frequency f_p . For instance, increasing the value of R_L up to 100 M Ω leads to a further increase of the SNR peak by a factor of 1.4. Thus, for these large values of R_L , the choice of the optimal operating frequency for QEPAS is not very critical, in case of a narrow-band LIA filter.

When a wider LPF bandwidth of the LIA is employed (e.g., bandwidth of 5 Hz), the SNR peak as a function of the operating frequency is still placed at f_s for small values of R_L , as in the case of narrow-band filter (see Figure 19). For large values of R_L , the SNR peak at f_p tends to be sharper as compared to the case of narrow-band LIA filter, thus the operating frequency for the QEPAS technique must be chosen as close as possible to f_p to maximize SNR. As an example, for $R_L = 100 \text{ M}\Omega$, the SNR peak is 1.4 times higher with respect to $R_L = 10 \text{ M}\Omega$.

In addition, the parallel-resonant frequency f_p of the QTF depends on the input capacitance of the OPAMP, so it is not an intrinsic property of the sensitive element. Thus, suitable techniques must be used to measure f_p in presence of C_{in} to exploit large values of R_L , increase SNR, and optimize the performance of the QEPAS sensor, especially when short acquisition times are needed. Instead, for long acquisition times, large values of R_L are not very effective for the increase of the overall SNR, and an accurate setting of the operating frequency close to f_s is not critical because of the flatness of SNR as a function of f_{op} . Of course, the value of R_L cannot be made too large, since the input bias current of the OPAMP would cause unacceptable input offset levels. All the results obtained with the previous analysis have been confirmed by AC and noise SPICE simulations of the voltage preamplifier followed by a band-pass filter with center frequency f_{op} and variable bandwidth.

Since, in QEPAS applications, several QTFs have been employed [1–14], the same study has also been carried out for a representative QTF characterized by an $f_s = 12.484 \text{ kHz}$ and a quality factor of 10^4 [9], and the same results were found.

The reported voltage amplifier, implementing the AD8067, will be employed to validate the results obtained both with our model and with the SPICE simulation.

Author Contributions: Conceptualization, M.D.G., G.M. (Giansergio Menduni), P.P. and V.S.; methodology, L.L., C.M. and G.M. (Giansergio Menduni); validation, M.D.G. and G.M. (Gianvito Matarrese); formal analysis, M.D.G., L.L. and C.M.; writing—original draft preparation, C.M.; writing—review and editing, M.D.G., L.L., Giansergio Menduni and P.P.; visualization, L.L., G.M. (Giansergio Menduni) and G.M. (Gianvito Matarrese); supervision, C.M., P.P. and V.S.; project administration, P.P. and V.S.; funding acquisition, V.S. All authors have read and agreed to the published version of the manuscript.

Funding: All authors acknowledge funding from the European Union’s Horizon 2020 research and innovation program under grant agreement No. 101016956 PASSEPARTOUT, in the context of the “INDUSTRIAL LEADERSHIP—Leadership in enabling and industrial technologies - Information and Communication Technologies (ICT)”.

Data Availability Statement: Not applicable.

Conflicts of Interest: The authors declare no conflict of interest.

References

1. Olivieri, M.; Menduni, G.; Giglio, M.; Sampaolo, A.; Patimisco, P.; Wu, H.; Dong, L.; Spagnolo, V. Characterization of H₂S QEPAS detection in methane-based gas leaks dispersed into environment. *Photoacoustics* **2023**, *29*, 100438. [[CrossRef](#)]
2. Lin, H.; Liu, Y.; Lin, L.; Zhu, W.; Zhou, X.; Zhong, Y.; Giglio, M.; Sampaolo, A.; Patimisco, P.; Tittel, F.K.; et al. Application of standard and custom quartz tuning forks for quartz-enhanced photoacoustic spectroscopy gas sensing. *Appl. Spectrosc. Rev.* **2022**, *57*, 1–23. [[CrossRef](#)]
3. Menduni, G.; Zifarelli, A.; Sampaolo, A.; Patimisco, P.; Giglio, M.; Amoroso, N.; Wu, H.; Dong, L.; Bellotti, R.; Spagnolo, V. High-concentration methane and ethane QEPAS detection employing partial least squares regression to filter out energy relaxation dependence on gas matrix composition. *Photoacoustics* **2022**, *26*, 100349. [[CrossRef](#)]
4. Yin, X.; Gao, M.; Miao, R.; Zhang, L.; Zhang, X.; Liu, L.; Shao, X.; Tittel, F.K. Near-infrared laser photoacoustic gas sensor for simultaneous detection of CO and H₂S. *Opt. Express.* **2021**, *29*, 34258. [[CrossRef](#)]
5. Ma, Y.; Lewicki, R.; Rzeghi, M.; Tittel, F.K. QEPAS based ppb-level detection of CO and N₂O using a high power CW DFB-QCL. *Opt. Exp.* **2013**, *21*, 1008–1019. [[CrossRef](#)]
6. Ma, Y. Review of Recent Advances in QEPAS-Based Trace Gas Sensing. *Appl. Sci.* **2018**, *8*, 1822. [[CrossRef](#)]
7. Wu, H.; Dong, L.; Zheng, H.; Yu, Y.; Ma, W.; Zhang, L.; Yin, W.; Xiao, L.; Jia, S.; Tittel, F.K. Beat frequency quartz-enhanced photoacoustic spectroscopy for fast and calibration-free continuous trace-gas monitoring. *Nat. Commun.* **2017**, *8*, 15331. [[CrossRef](#)]
8. Liu, Y.; Lin, H.; Montano, B.A.Z.; Zhu, W.; Zhong, Y.; Kan, R.; Yuan, B.; Yu, J.; Shao, M.; Zheng, H. Integrated near-infrared QEPAS sensor based on a 28 kHz quartz tuning fork for online monitoring of CO₂ in the greenhouse. *Photoacoustics* **2022**, *25*, 100332. [[CrossRef](#)]
9. Menduni, G.; Zifarelli, A.; Kniazeva, E.; Dello Russo, S.; Ranieri, A.C.; Ranieri, E.; Patimisco, P.; Sampaolo, A.; Giglio, M.; Manassero, F.; et al. Measurement of methane, nitrous oxide and ammonia in atmosphere with a compact quartz-enhanced photoacoustic sensor. *Sens. Actuators B Chem.* **2023**, *375*, 132953. [[CrossRef](#)]
10. Zifarelli, A.; De Palo, R.; Patimisco, P.; Giglio, M.; Sampaolo, A.; Blaser, S.; Butet, J.; Landry, O.; Müller, A.; Spagnolo, V. Multi-gas quartz-enhanced photoacoustic sensor for environmental monitoring exploiting a Vernier effect-based quantum cascade laser. *Photoacoustics* **2022**, *28*, 100401. [[CrossRef](#)]
11. Liberatore, N.; Viola, R.; Mengali, S.; Masini, L.; Zardi, F.; Elmi, I.; Zampolli, S. Compact GC-QEPAS for On-Site Analysis of Chemical Threats. *Sensors* **2023**, *23*, 270. [[CrossRef](#)]
12. Zifarelli, A.; Menduni, G.; Giglio, M.; Elefante, A.; Sukhinets, A.; Sampaolo, A.; Patimisco, P.; Fangyuan, S.; Chongwu, W.; Wang, Q.J.; et al. Compact and versatile QEPAS-based sensor box for simultaneous detection of methane and infrared absorber gas molecules in ambient air. *Front. Environ. Chem.* **2022**, *3*, 926233. [[CrossRef](#)]
13. Li, B.; Feng, C.; Wu, H.; Jia, S.; Dong, L. Calibration-free mid-infrared exhaled breath sensor based on BF-QEPAS for real-time ammonia measurements at ppb level. *Sens. Actuators B Chem.* **2022**, *358*, 131510. [[CrossRef](#)]
14. Shang, Z.; Li, S.; Li, B.; Wu, H.; Sampaolo, A.; Patimisco, P.; Spagnolo, V.; Dong, L. Quartz-enhanced photoacoustic NH₃ sensor exploiting a large-prong-spacing quartz tuning fork and an optical fiber amplifier for biomedical applications. *Photoacoustics* **2022**, *26*, 100363. [[CrossRef](#)] [[PubMed](#)]
15. Dello Russo, S.; Sampaolo, A.; Patimisco, P.; Menduni, G.; Giglio, M.; Hoelzl, C.; Passaro, V.M.N.; Wu, H.; Dong, L.; Spagnolo, V. Quartz-enhanced photoacoustic spectroscopy exploiting low-frequency tuning forks as a tool to measure the vibrational relaxation rate in gas species. *Photoacoustics* **2021**, *21*, 100227. [[CrossRef](#)]
16. Kosterev, A.A.; Bakhrin, Y.A.; Curl, R.F.; Tittel, F.K. Quartz-enhanced photoacoustic spectroscopy. *Opt. Lett.* **2002**, *27*, 1902–1904. [[CrossRef](#)]
17. Kosterev, A.A.; Tittel, F.K.; Serebryakov, D.; Malinovsky, A.; Morozov, A. Applications of quartz tuning fork in spectroscopic gas sensing. *Rev. Sci. Instrum.* **2005**, *76*, 043105. [[CrossRef](#)]
18. Menduni, G.; Sampaolo, A.; Patimisco, P.; Giglio, M.; Dello Russo, S.; Zifarelli, A.; Elefante, A.; Wiczorek, P.Z.; Starecki, T.; Passaro, V.M.N.; et al. Front-End Amplifiers for Tuning Forks in Quartz Enhanced PhotoAcoustic Spectroscopy. *Appl. Sci.* **2020**, *10*, 2947. [[CrossRef](#)]
19. Wiczorek, P.Z.; Starecki, T.; Tittel, F.K. Improving the signal to noise ratio of QTF preamplifiers dedicated for QEPAS applications. *Appl. Sci.* **2020**, *10*, 4105. [[CrossRef](#)]
20. Winkowski, M.; Stacewicz, T. Low noise, open-source QEPAS system with instrumentation amplifier. *Sci. Rep.* **2019**, *9*, 7–12. [[CrossRef](#)]
21. Starecki, T.; Wiczorek, P.Z. A High Sensitivity Preamplifier for Quartz Tuning Forks in QEPAS (Quartz Enhanced PhotoAcoustic Spectroscopy) Applications. *Sensors* **2017**, *17*, 2528. [[CrossRef](#)]

22. Principles of Lock-in Detection and the State of the Art, Zurich Instruments. Available online: https://www.zhinst.com/sites/default/files/documents/2020-06/zi_whitepaper_principles_of_lock-in_detection.pdf (accessed on 19 January 2023).
23. Kishore, K.; Akbar, S.A. Evolution of Lock-In Amplifier as Portable Sensor Interface Platform: A Review. *IEEE Sens. J.* **2020**, *20*, 10345–10354. [[CrossRef](#)]
24. Zhang, Z.; Li, C.; Huang, Z. Quadrature demodulation based on lock-in amplifier technique for self-mixing interferometry displacement sensor. *Appl. Opt.* **2019**, *58*, 6098–6104. [[CrossRef](#)]
25. Huang, K.; Geng, Y.; Zhang, X.; Chen, D.; Cai, Z.; Wang, M.; Zhu, Z.; Wang, Z. A Wide-Band Digital Lock-In Amplifier and Its Application in Microfluidic Impedance Measurement. *Sensors* **2019**, *19*, 3519. [[CrossRef](#)] [[PubMed](#)]
26. Patimisco, P.; Scamarcio, G.; Tittel, F.K.; Spagnolo, V. Quartz-Enhanced Photoacoustic Spectroscopy: A Review. *Sensors* **2014**, *14*, 6165–6206. [[CrossRef](#)]
27. Levy, R.; Duquesnoy, M.; Melkonian, J.-M.; Raybaut, M.; Aoust, G. New Signal Processing for Fast and Precise QEPAS Measurements. *IEEE Trans. Ultrason. Ferroelectr. Freq. Control* **2020**, *67*, 1230–1235. [[CrossRef](#)]
28. Serebryakov, D.V.; Cherkun, A.P.; Loginov, B.A.; Letokhov, V.S. Tuning-fork-based fast highly sensitive surface-contact sensor for atomic force microscopy/near-field scanning optical microscopy. *Rev. Sci. Instrum.* **2002**, *73*, 1795. [[CrossRef](#)]
29. Friedt, J.-M.; Carry, É. Introduction to the quartz tuning fork. *Am. J. Phys.* **2007**, *75*, 415–422. [[CrossRef](#)]
30. The Quartz Crystal Model and Its Frequencies. Technical Note 32, Rev. A. *Statek*. Available online: <https://statek.com/wp-content/uploads/2018/03/tn32.pdf> (accessed on 19 January 2023).
31. AD8067, High Gain Bandwidth Product, Precision Fast FET™ Op Amp. Analog Devices Inc. Available online: <https://www.analog.com/en/products/ad8067.html> (accessed on 19 January 2023).
32. Noise Analysis in Operational Amplifier Circuits, Application Report. Texas Instruments. Available online: <https://www.ti.com/lit/an/slva043b/slva043b.pdf> (accessed on 19 January 2023).
33. Current Noise in FET Input Amps. Analog Devices Inc. Available online: <https://www.analog.com/en/analog-dialogue/raqs/raq-issue-174.html> (accessed on 19 January 2023).
34. Sedra, A.S.; Smith, K.C. *Microelectronic Circuits*, 6th ed.; Oxford University Press: Oxford, UK, 2010; pp. 975–982.
35. Villa, T.F.; Salimi, F.; Morton, K.; Morawska, L.; Gonzalez, F. Development and Validation of a UAV Based System for Air Pollution Measurements. *Sensors* **2016**, *16*, 2202. [[CrossRef](#)] [[PubMed](#)]
36. Aasen, H.; Honkavaara, E.; Lucieer, A.; Zarco-Tejada, P.J. Quantitative Remote Sensing at Ultra-High Resolution with UAV Spectroscopy: A Review of Sensor Technology, Measurement Procedures, and Data Correction Workflows. *Remote Sens.* **2018**, *10*, 1091. [[CrossRef](#)]

Disclaimer/Publisher’s Note: The statements, opinions and data contained in all publications are solely those of the individual author(s) and contributor(s) and not of MDPI and/or the editor(s). MDPI and/or the editor(s) disclaim responsibility for any injury to people or property resulting from any ideas, methods, instructions or products referred to in the content.